RESEARCH ARTICLE | APRIL 22 2025

High-order resonance enhancing the mass sensitivity of diamond cantilevers

Special Collection: Ultrawide Bandgap Semiconductors

Wen Zhao ; Guo Chen ; Keyun Gu ; Masaya Toda; Yasuo Koide ; Meiyong Liao

APL Mater. 13, 041124 (2025)
https://doi.org/10.1063/5.0250902

High-order resonance enhancing the mass sensitivity of diamond cantilevers

Cite as: APL Mater. 13, 041124 (2025); doi: 10.1063/5.0250902
Submitted: 28 November 2024 • Accepted: 8 April 2025 •
Published Online: 22 April 2025

Wen Zhao,[1] Guo Chen,[1] Keyun Gu,[1] Masaya Toda,[2] Yasuo Koide,[1] and Meiyong Liao[1,a)]

AFFILIATIONS

[1] Research Center for Electronic and Optical Materials, National Institute for Materials Science, Namiki 1-1, Tsukuba, Ibaraki 305-0044, Japan
[2] Graduate School of Engineering, Tohoku University, Sendai, Miyagi 9808579, Japan

Note: This paper is part of the Special Topic on Ultrawide Bandgap Semiconductors.
[a)] **Author to whom correspondence should be addressed:** meiyong.liao@nims.go.jp

ABSTRACT

Diamond has been demonstrated as an exceptional semiconductor for microelectromechanical system (MEMS) sensors, offering high sensitivity and reliability due to its ultra-wide bandgap energy, superior mechanical properties, and high thermal conductivity. For MEMS resonator-type sensors that rely on frequency shift detection, such as mass sensors, the overall performance, including the sensitivity, speed, resolution, and noise level, is collectively determined by the stability of the resonance frequency. To improve the sensing performance, geometry optimization and nonlinear operation methods have been used, but these methods lead to increased fabrication complexity or increased energy dissipation. In this work, we propose the utilization of high-order resonance modes to enhance the resonance frequency stability of single-crystal diamond (SCD) MEMS resonators, achieving a significant improvement in mass resolution to as low as 0.15 atto-grams at room temperature. This approach offers a streamlined and competitive strategy for advancing the sensing capabilities of MEMS sensors.

I. INTRODUCTION

Microelectromechanical system (MEMS) resonant microbeams, due to their small size, low power consumption, and high sensitivity, have garnered significant attention for high-resolution sensing applications,[1–6] including biological detection,[7–9] environmental monitoring,[10,11] and physical characterization.[12,13]

The sensing performance of these advanced sensors is predominantly determined by their frequency stability when the external quantities are detected by the resonance frequency shift. In many cases, the sensing mechanism relies on detecting a mass change induced by the target, which manifests as a resonance shift in amplitude-frequency response.[14,15] In such a case, the resolution of the resonant-type MEMS sensor is governed by the relation $\Delta m/m = 2\Delta f/f_0$, where Δm represents the mass resolution, m is the effective mass of the resonator, Δf denotes the frequency shift, and f_0 is the resonance frequency of the resonator. This equation highlights two primary approaches to enhance mass resolution: reducing $\Delta f/f_0$ or decreasing the effective mass m of the resonator.

Achieving high frequency stability favors a high quality (Q) factor,[16] which can be enhanced through stain dilution techniques.[17] Another approach to improving mass resolution is miniaturizing the resonator to reduce its overall mass. However, extreme size reduction to nanoscale increases fabrication complexity and often leads to Q-factor degradation,[18–21] thereby compromising frequency stability and sensing performance. Another alternative and widely applicable strategy is to increase the resonance frequency f_0 without altering the resonator's mass. Operating at higher-order resonance modes, their shorter vibration period enables rapid response, effectively mitigating fluctuation-induced limitations. In addition, their increased stiffness makes the microsystem less sensitive to external environmental factors such as temperature fluctuations, further improving stability and reliability. In addition, when combined with a diamond MEMS resonator, the exceptional mechanical and thermal properties of diamond further enhance resonance frequency stability and mass sensitivity.[22–25] For example, diamond resonators possess a unique feature of low thermal coefficient of frequency (TCF), less than −10 ppm/K, which is better than −30 ppm/K of

silicon,[26] making diamond MEMS resonators less sensitive to thermal fluctuation.

In this work, we propose the utilization of higher-order resonance mode to enhance the frequency stability of single-crystal diamond (SCD) MEMS resonators. We focus on the first three resonant vibration modes, with frequency fluctuations tracked and analyzed at each mode by using Allan deviation, a standard metric for quantifying in precision measurements. Our findings reveal a substantial improvement in the evaluated mass resolution of the SCD MEMS resonator-based sensors, from 0.66 atto-gram (ag) for the first resonance mode to an impressive 0.15 ag for the third resonance mode.

II. EXPERIMENTS

We conducted the smart-cut technique to fabricate the SCD MEMS cantilever resonators.[27] The detailed fabrication process is demonstrated in Fig. 1(a), encompassing diamond growth, lithography, metal mask deposition, etching, and releasing. High-quality diamond epilayers were grown using microwave plasma chemical vapor deposition (CVD) on ion-implanted high-pressure, high-temperature (HPHT) type-Ib SCD substrates.[28,29] Ion implantation created a graphitized carbon layer, which was subsequently etched to facilitate the release of the cantilevers. Finally, the graphite layer was selectively removed without affecting the SCD epilayer. Once fully released, the diamond microcantilever resonator array was successfully fabricated. The dimensions of the fabricated cantilevers are a width of 6 μm and a length ranging from 180 to 40 μm, as shown in Fig. 1(b). It is noted that ion implantation can degrade device performance by introducing defects related energy dissipation. The device performance can be optimized by completely removing the damaged layer or by increasing the epilayer thickness.[30,31]

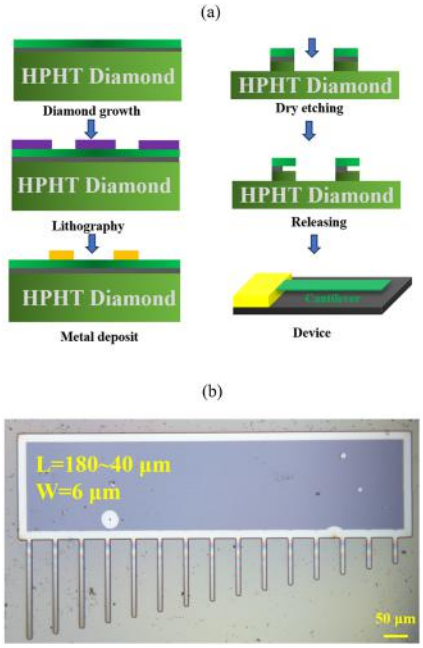

FIG. 1. (a) Fabrication procedure of the MEMS diamond cantilever resonator based on the smart-cut method. (b) Optical image of the fabricated SCD cantilever array.

A laser Doppler vibrometer (LDV) was used to measure the out-of-plane displacement and velocity.[32,33] The SCD cantilevers are actuated by a radio frequency (RF) signal from the lock-in amplifier, equipped with a phase locked loop (PLL), which is also used to investigate the frequency stability by tracking the frequency fluctuation over the time regime. The noise analysis is based on the theory of Allan deviation.[16,34] To efficiently reduce the air damping and enhance the Q factor, all the measurements were conducted in a very high vacuum chamber with a pressure less than the value of 10^{-4} Pa at room temperature. It is worth mentioning that all the displacement measurements are taken by positioning the laser spot at the tip of the microbeam (maximum displacement point) to achieve a high signal-to-noise ratio (SNR).[28]

III. RESULTS AND DISCUSSION

To examine the length effect on the resonance frequency of the SCD cantilever beams, we measured the first three modes of the cantilever beams by sweeping the excitation frequency around their corresponding resonance. Figure 2 illustrates the resonance frequency values of the first three modes of the SCD cantilevers as a dependence of the cantilever lengths (L) ranging from 40 to 180 μm. As shown in Fig. 3(a), the resonance frequencies decrease as the length increases due to the reduced effective stiffness for all three modes. Resonance frequencies exhibit a linear relationship with $1/L^2$, consistent with Euler–Bernoulli theory. The consistency between experiments and theory confirms the reproducibility of the current fabrication method for SCD MEMS structure fabrication and also reveals the availability of the obtained experimental data.

We focus on one typical SCD cantilever to investigate the resonance performance with a length L = 170 μm and a width w = 6 μm in Secs. IV A and IV B. First, to fully understand the resonance frequency of the micro-diamond cantilever beam, we first conduct the excitation frequency sweep around the first three modes under various actuation RF AC amplitudes, as shown in Figs. 3(a)–3(c), respectively. The resonance frequency and Q factor of the out-of-plane vibration motion are f_1 = 174.894 kHz and Q_1 ~ 14 015 for the first resonance mode, f_2 = 1087.301 kHz and Q_2 ~ 11 243 for the second resonance mode, and f_3 = 3018.439 kHz and Q_3 ~ 8300 for the third resonance mode.

The increased AC amplitude enhances the resonance vibration amplitude. For all modes, the actuation AC amplitude linearly increases the resonance vibration amplitudes, as illustrated in Fig. 4. The Q factors here for each mode are calculated based on the full width at half maximum (FWHM) and are also plotted in Fig. 4. The increased AC voltage has little effect on the Q factors due to the operation in the linear domain. Note that the calculated Q factors are obtained by Lorentz fitting of each frequency response, and each value is marked in corresponding plots. In addition, the Q-factor decreases with the increased mode number due to the high energy dissipation induced by the damping ratio of higher order modes. Higher-order modes (HOMs) exhibit increasingly complex mode

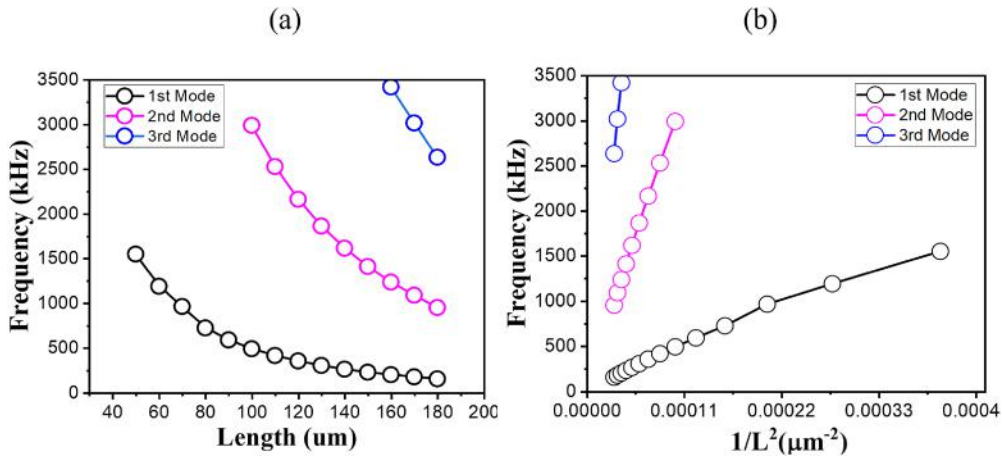

FIG. 2. (a) Dependence of the resonance frequency on the cantilever length at the first three modes. (b) Linear fitting of the measured resonance frequency with $1/L^2$ on the first three modes.

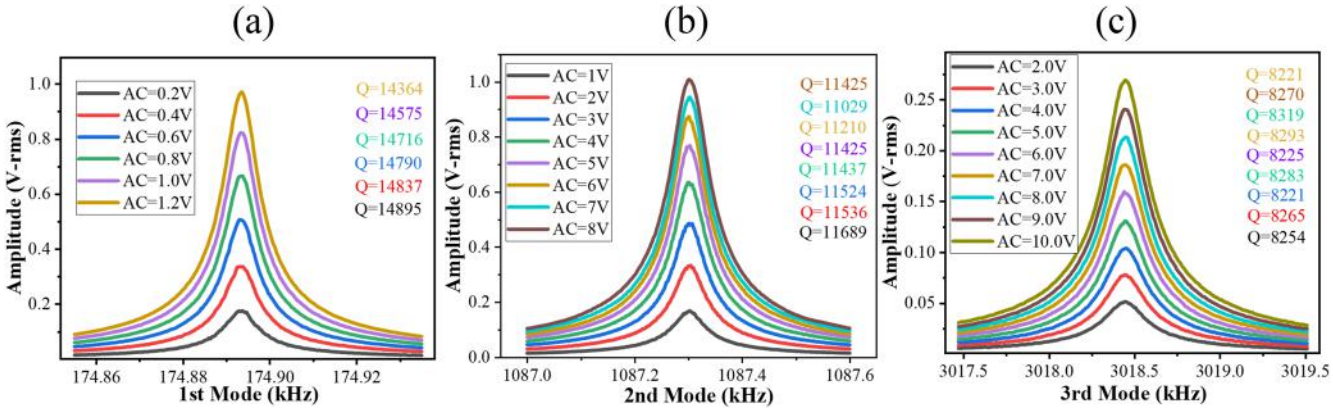

FIG. 3. First three mode responses: (a) first mode, (b) second mode, and (c) third mode.

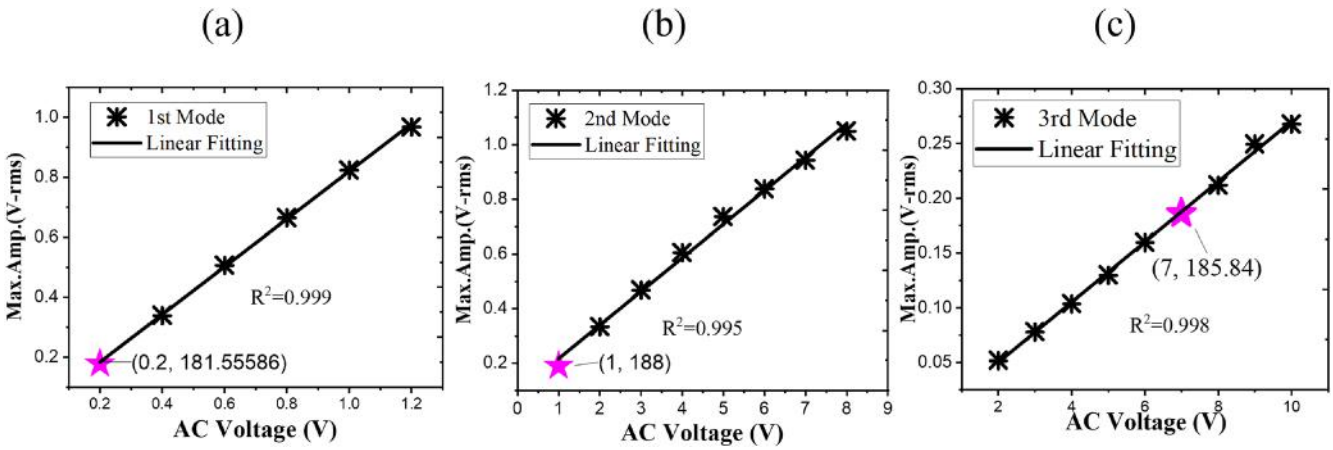

FIG. 4. Resonance frequency spectra and Q-factor of the first three modes under different AC voltages for the SCD cantilever with a length of 170 μm: (a) first mode, (b) second mode, and (c) third mode. The marked point as the star has a similar signal-to-noise ratio (SNR) in each mode and is used to compare the frequency stability in Sec. III.

TABLE I. Values of a quality factor with actuated modes of MEMS cantilever beams with various lengths.

	Q1	Q2	Q3
Cantilever length (L) (μm)	(first mode)	(second mode)	(third mode)
180	13 965	10 402	5088
170	14 696	11 409	8261
160	15 047	10 330	
150	13 345	10 867	
140	14 992	11 574	
130	14 911	9966	
120	14 098	8346	NA
110	14 385	8701	
100	12 012	7739	
90	12 143	8388	
80	12 764		
70	12 757	NA	
60	10 776		

shapes, generating multiple nodal regions along the beam length for different vibration modes. First, these nodal regions lead to highly localized strain distributions, amplifying internal friction losses and consequently reducing the Q-factor. Second, the intricate vibration profiles of HOMs could induce stronger anchor interactions and enhance thermoelastic damping due to the rapid cyclic compression and expansion of the resonator. As a result, the Q-factor decreases as the mode order increases.

To further examine the length-dependent Q-factor, we briefly illustrate the Q-factor values of the cantilever beams with lengths ranging from 60 to 180 μm in Table I. The results indicate that the Q factors show little independence on the beam lengths for L > 100 μm. The clamping loss becomes dominant for the cases with L less than 60 μm, consistent with our previous study.[35] It is noted that the Q-factor determines the minimum detectable frequency shift, which directly affects the short-term stability of the resonator.[16,36] A higher Q-factor can reduce noise and improves frequency stability, thereby lowering the Allan deviation at short integration times.

IV. FREQUENCY STABILITY

We utilize Allan deviation to analyze the frequency stability, which is mathematically quantified as[16,34]

$$\sigma(\tau) = \sqrt{\frac{1}{2(N-1)} \sum_{i=1}^{N-1} \left(\frac{\bar{f}_{i+1} - \bar{f}_i}{\bar{f}_0} \right)^2}, \quad (1)$$

where N is the number of samples of the resonance frequency $f_1 \ldots f_N$, each with averaged integration time τ within a total of N intervals. f_0 is the reference resonance frequency. Measurements here for Allan analysis are made in the closed-loop configuration by tracking the frequency fluctuation within 5 min in the lock-in amplifier. The sampling rate is set to be 1799 Sa/s for all frequency fluctuation measurements.

A. Fundamental mode (first mode)

We first investigate the frequency stability of the first resonance mode using the phase locked loop (PLL) circuit at different bandwidths (BWs) of 1, 50, 100, and 400 Hz, as shown in Figs. 5(a)–5(d). The frequency stability under different actuation AC amplitudes was characterized. The signal-to-noise ratio (SNR) is controlled through variation in the applied voltages, which increases with the vibrational amplitude. An order of magnitude reduction of $\sigma(\tau)$ is clearly observed for lower BW = 1 Hz compared with that of BW = 100 Hz. Due to the large sampling rates (1799 Sa/s), we can also detect the involved noise from the measurement system. The results indicate that the noise is mainly dominated by detection and thermomechanical noise together, especially in the case with a lower BW. The closed-loop response time relies on the bandwidth value in the phase locked loop (PLL) system instead of the intrinsic response time of the target resonator in our case. Apparently, the reduced bandwidth can significantly enhance the minimal detection. In the case of BW = 1 Hz, the minimal detection can reach $\sigma(\tau) \sim 2.6 \times 10^{-8}$, for the first mode. When enlarging the bandwidth of the PLL, the point of transition between detection noise and thermomechanical noise changes to the lower value of integration time τ, that is, because higher BW allows more high-frequency detection noise, raising the initial Allan deviation at short integration times. In addition, the thermomechanical noise starts to dominate over the detection noise during the evolution of Allan deviation. For example, in the case of BW = 400 Hz in Fig. 5(d), the system noise from the starting point is buried in Allan deviation, while the thermomechanical noise dominates overall. For the time constant of the PLL (lower BW) lower than the resonator response time, the detection noise limit is smaller. The filter from the PLL, in addition to the filtering by the intrinsic response of the resonator and the demodulator filter, reduces the $\sigma(\tau)$ of the system.[37]

To further clarify the BW effect, we specifically investigate several cases with different BWs for a high SNR measured at AC = 1.0 V, as shown in Fig. 6(a). The increased bandwidth shortens the transition time from detection noise to thermomechanical noise. In addition, the obtained experimental results further confirm that the minimum detection value is not influenced by the bandwidth. This is attributed to the phase-locked loop (PLL) bandwidth being configured to accommodate frequency signals within the designated signal bandwidth, ensuring accurate frequency tracking without compromising sensitivity. We plot the minimal detection value of frequency relativity at BW = 100 Hz by varying the applied AC voltage, as shown in Fig. 6(b). When increasing the AC volts ranging from 0.2 to 1.0 V, the minimal detection can be highly improved due to a larger SNR value in amplitude–frequency response. In addition, it is noticeable that applying an excessively large AC voltage to drive a microdevice can induce pull-in instability, a nonlinear phenomenon that causes the microresonator to come into contact with the substrate. As a result, the minimal detection value (fundamental limits) saturates and becomes largely independent of the applied voltage.

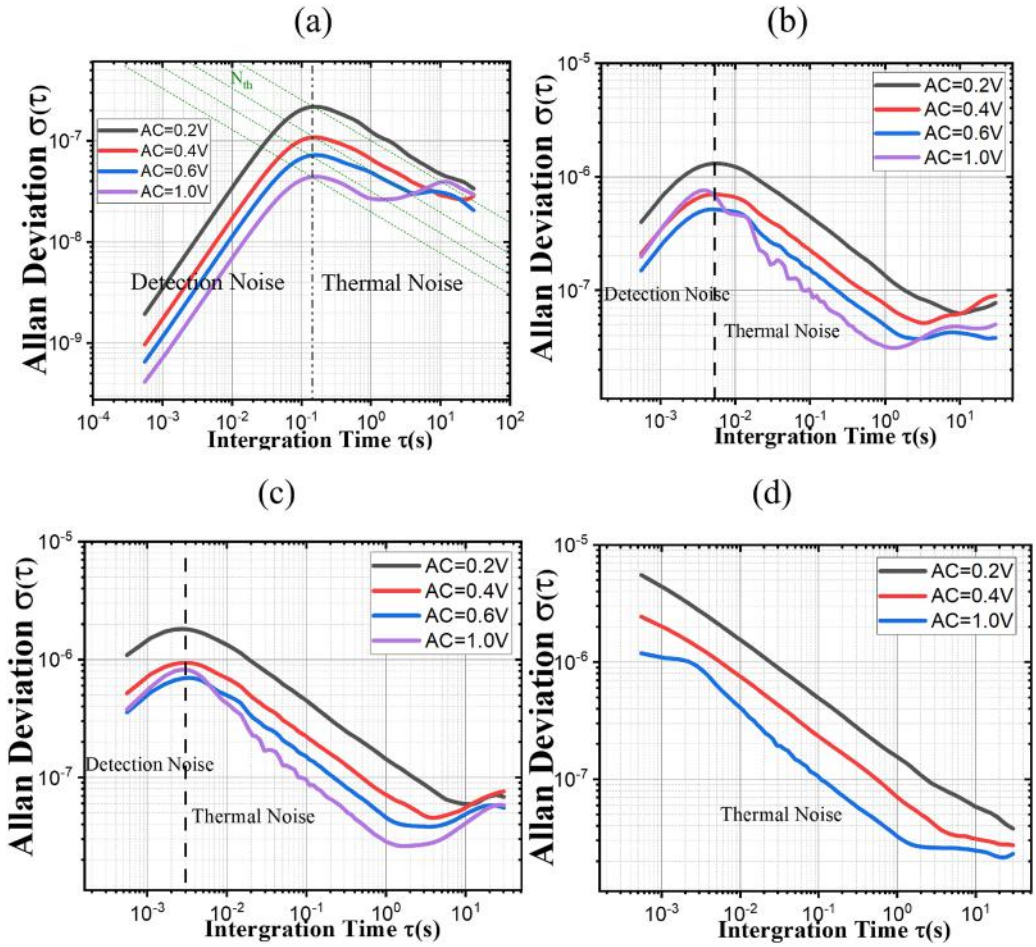

FIG. 5. AC voltage effects of varying noise on Allan deviation, for the first mode, at (a) BW = 1 Hz, (b) BW = 50 Hz, (c) BW = 100 Hz, and (d) BW = 400 Hz. The thermal noise limit (green dashed line, Nth) and detection noise limits (red dashed line, N_d), calculated based on Ref. 16, are marked in (a). It is worth mentioning that the detection noise limits from the testing instruments can be captured when increasing the sampling rate to at least 10^4 Sa/s.

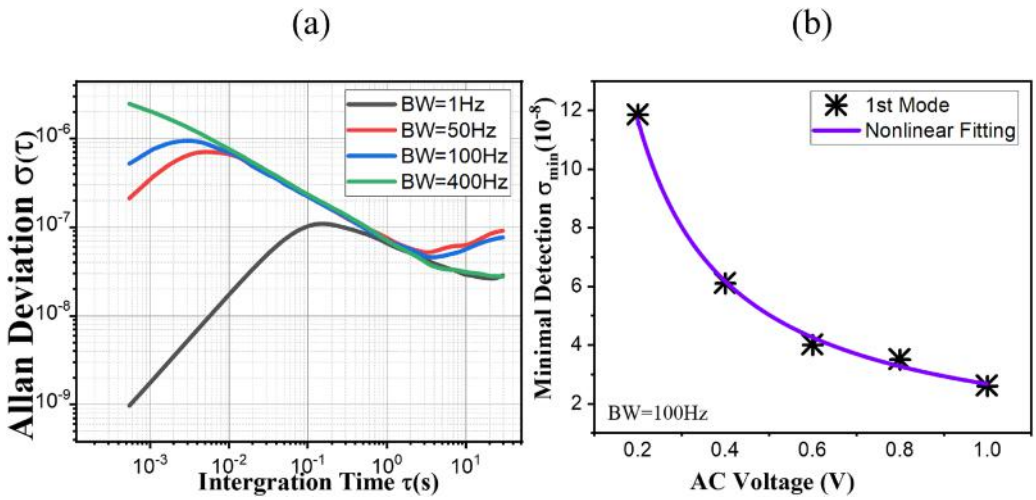

FIG. 6. (a) BW effects of varying noise on Allan deviation at AC = 0.4 V for the first mode; (b) AC effects on the minimal detection at the first mode.

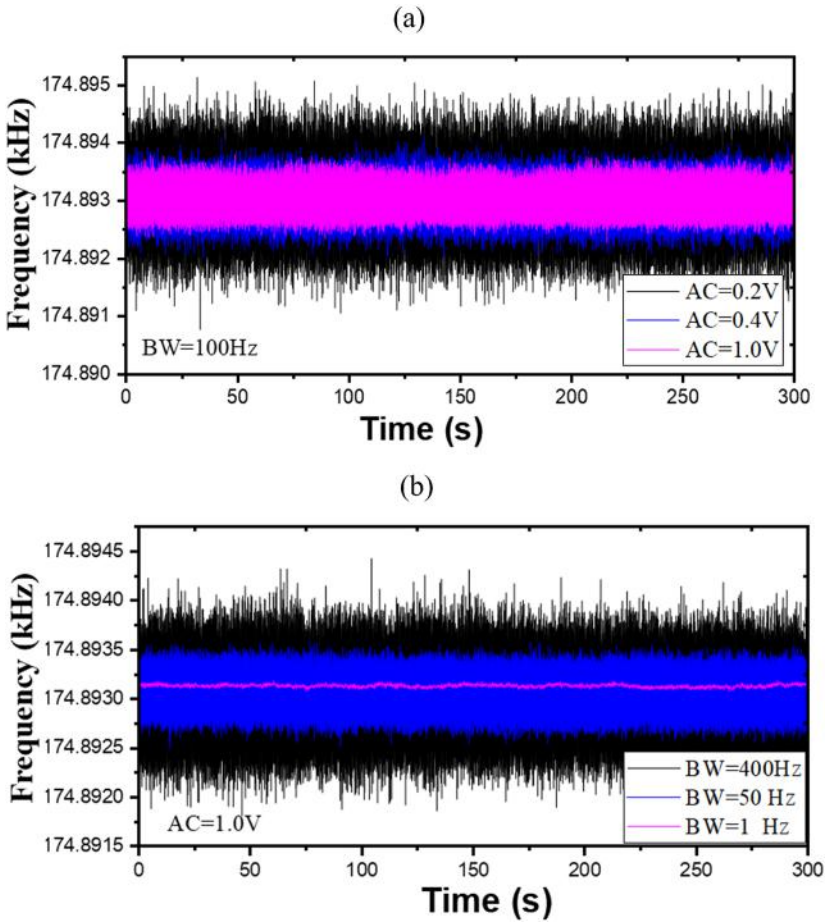

FIG. 7. First resonance mode fluctuation over the time domain. (a) AC effects at BW = 100 Hz and (b) BW effects at AC = 1.0 V.

To better illustrate how the AC and BW affect the frequency stability in the time domain, we plot the first resonance mode fluctuation over the time with varying AC voltages and bandwidths in Fig. 7. Notably, the resonance mode fluctuation remains stable over the investigated period (5 min). Increasing AC voltage within the linear frequency response domain reduces frequency fluctuations, improving the frequency stability due to the higher SNR, which makes the resonance less susceptible to noise-induced variations. In addition, a smaller BW acts as a filter, effectively attenuates various types of involved noise, and contributes to a more stable frequency response.

B. Higher order modes (second and third modes)

Higher-order modes normally exhibit higher resonance frequencies, a wide dynamic range, high sensitivity, and fast response time. In this section, we mainly investigate the frequency stability of the second mode and the third mode due to the upper-frequency limit of our LDV measurement system based on the Allan deviation.

Figures 8(a)–8(d) illustrate the impact of different bandwidths (1, 50, 100, and 400 Hz) on Allan deviation for the second resonance mode under various applied AC amplitudes. The obtained results indicate that both detection (facility) noise and thermomechanical noise dominate over the overall responses, similar to the first mode resonance. In particular, the detection noise dominates for a lower bandwidth [Fig. 8(a)], while thermochemical noise dominates at a higher bandwidth [Fig. 8(d)]. With the transition between detection noise and thermomechanical noise down to the lower time regime, larger bandwidths can mitigate the effect of detection noise. By closer observation, the minimal detection value is highly enhanced by the increased AC voltage due to the large dynamic response; at a bandwidth of 1 Hz, the minimal detection value reaches $\sigma(\tau) = 1.21 \times 10^{-8}$ for the second mode, slightly lower than that of the first resonance mode [$\sigma(\tau) = 2.62 \times 10^{-8}$].

In Figs. 9(a)–9(c), we illustrate the bandwidth effects on the frequency stability at the various applied AC voltages. It is evident that the increased BW shortens the transition time between detection noise and thermomechanical noise. For higher BW, the detection noise eventually disappears, similar to that of the first resonance

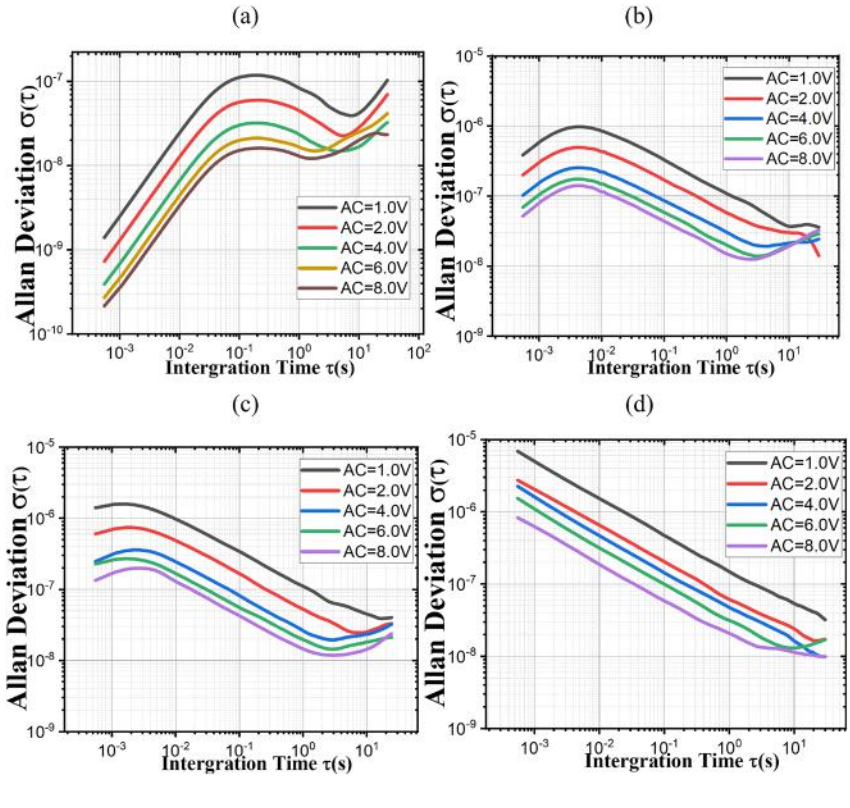

FIG. 8. AC voltage effects of varying noise on Allan deviation, for the second mode, at (a) BW = 1 Hz, (b) BW = 50 Hz, (c) BW = 100 Hz, and (d) BW = 400 Hz.

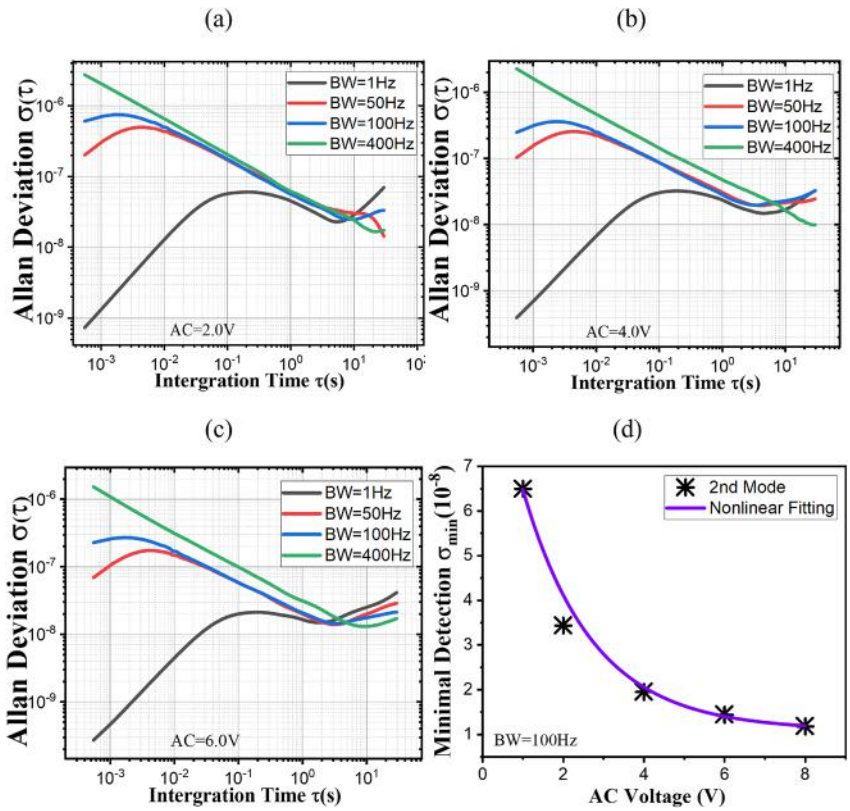

FIG. 9. Bandwidth effects of varying noise on Allan deviation, for the second mode, at (a) AC = 2.0 V, (b) AC = 4.0 V, and (c) AC = 6.0 V; (d) applied AC effects on the minimal detection at the first mode when BW = 100 Hz.

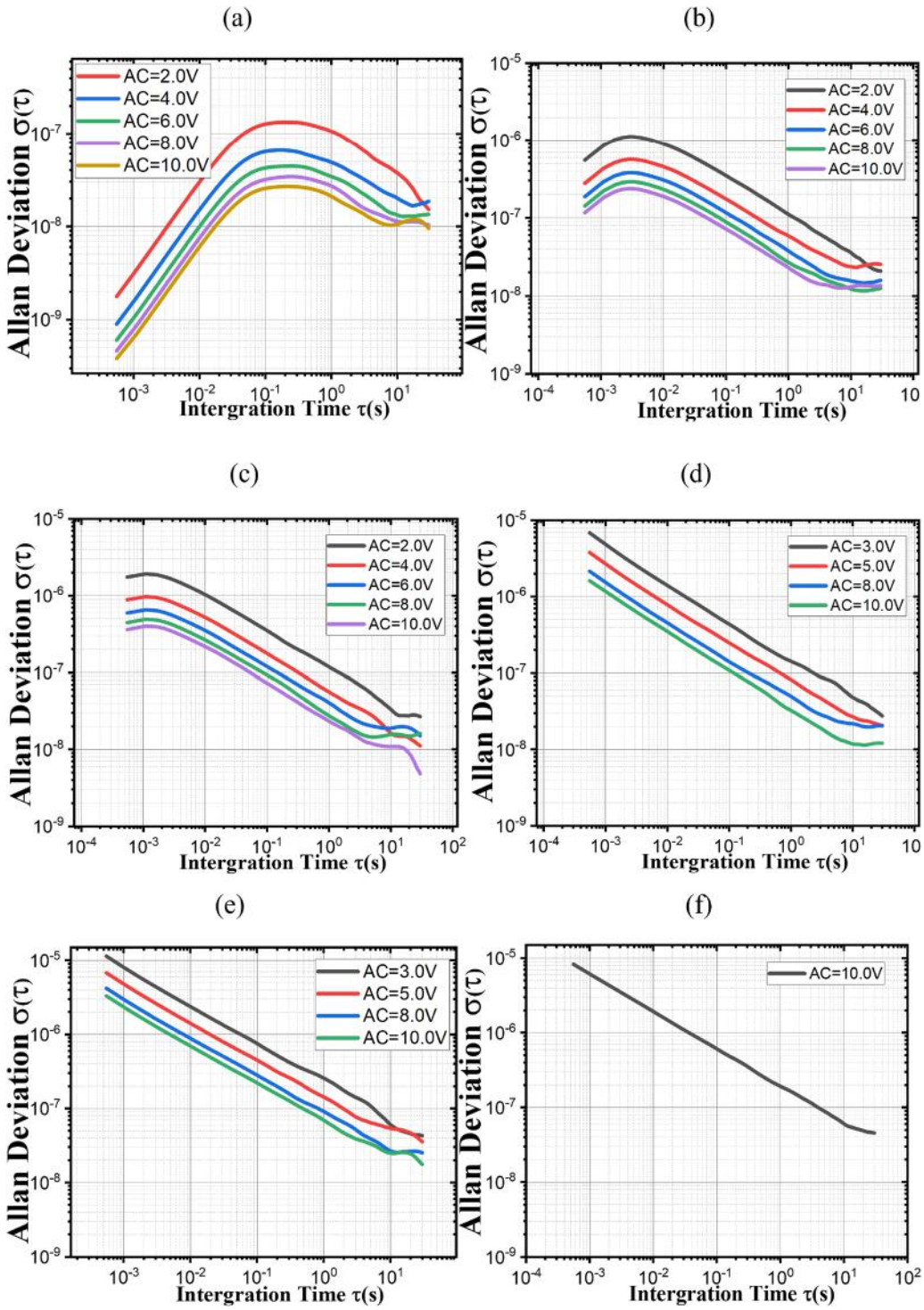

FIG. 10. Actuation RF AC voltage effects of varying noise on Allan deviation, for the third mode, at (a) BW = 1 Hz, (b) BW = 50 Hz, (c) BW = 100 Hz, (d) BW = 400 Hz, (e) BW = 500 Hz, and (f) BW = 1000 Hz.

mode. A closer analysis in Fig. 9(d) shows that the minimal detection value continues to decrease with increasing AC voltage, further enhancing the sensor's performance.

Similarly, we analyze the frequency stability of the third mode with a resonance frequency of f_3 = 3018.439 kHz, as shown in Figs. 10 and 11. Similar to the previous modes, increasing the AC voltage leads to a reduction in the magnitude of σ(τ), with detection noise remaining at a low level. As the bandwidth in the PLL is broadened, detection noise gradually disappears, and thermomechanical noise becomes dominant. However, compared to the results of the first mode, higher-order mode resonance significantly reduces noise constraints because the increased resonance frequency results in a larger relative frequency shift ($\Delta f/f_0$) compared to the fundamental mode, resulting in a marked improvement in minimal force detection and mass resolution.

Based on the formula for mass sensing, $\Delta f = (f_0/2m_0) \times \Delta m$,[38] the mass resolution significantly improves to 1.5×10^{-19} g (0.15 ag) for the third resonance mode from $6.6 \times 10^{-1}9$ g (0.66 ag) for the first resonance mode by utilizing higher order modes for mass sensing.

To further elucidate the advantage of higher-order modes, we compare amplitude–frequency response of the first three modes under the same signal-to-noise ratio conditions in the linear domain, as shown in Figs. 12(a)–12(c). The comparison highlights the enhanced stability provided by higher-order modes actuation. As a result, the diamond resonator's mass detection capability is enhanced from 0.66 ag for the first resonance mode to 0.15 attogram (ag) for the third resonance mode, surpassing that of the previous report (1.4 ag),[39] as listed in Table II. Therefore, it is a clear assessment of how higher-order modes outperform fundamental modes in terms of sensing performance and frequency stability.

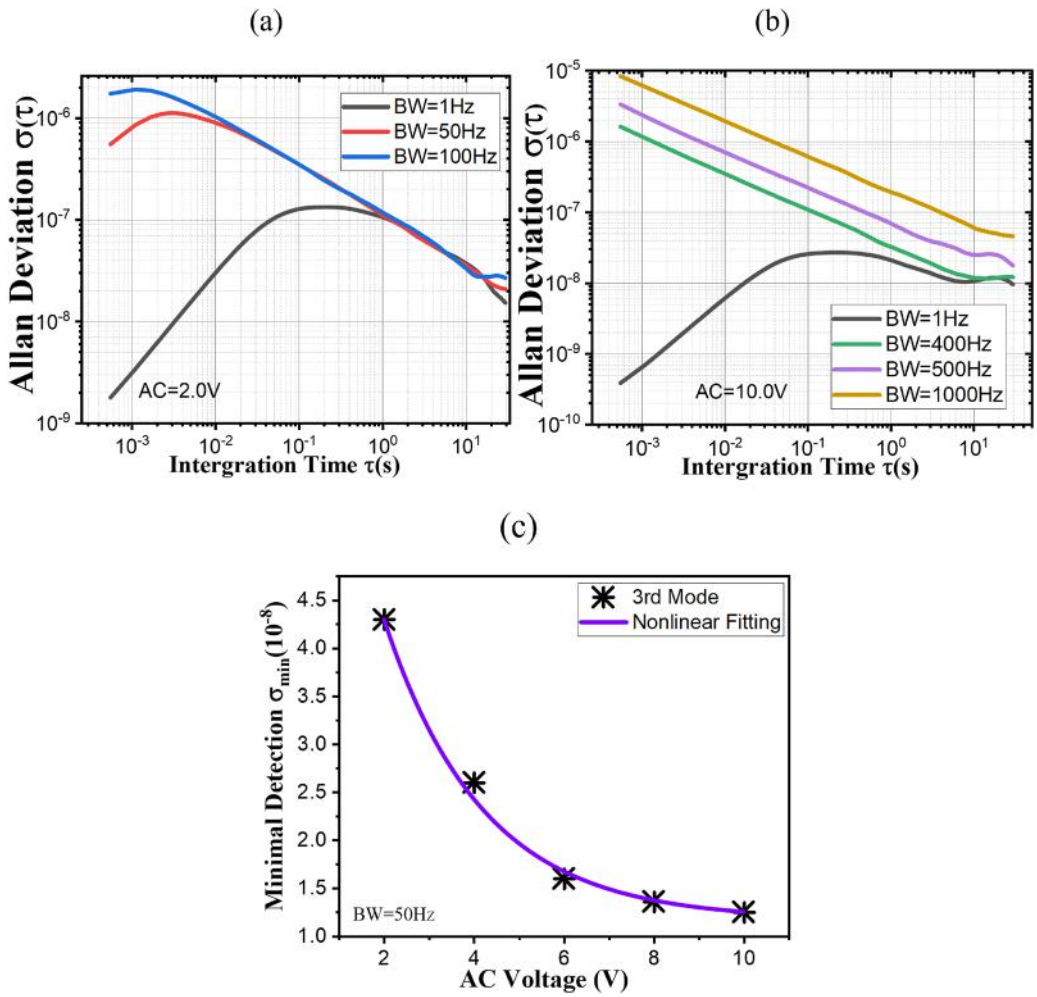

FIG. 11. BW effects on Allan deviation, for the third mode, at (a) AC = 2.0 V and (b) AC = 10.0 V; (c) applied AC effects on the minimal detection at the first mode when BW = 100 Hz.

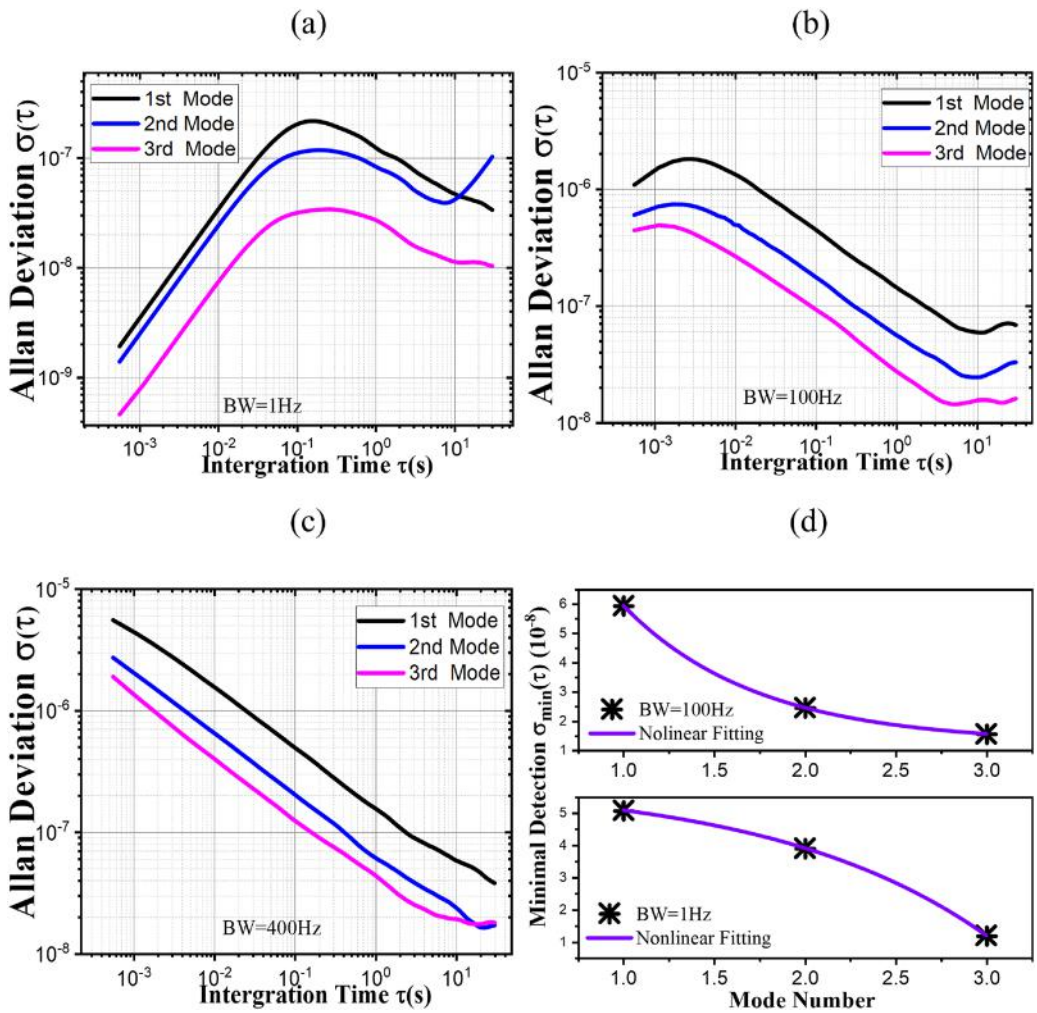

FIG. 12. BW effects of varying noise on normalized results of Allan deviation under different resonant modes (a) BW = 1 Hz, (b) BW = 1 Hz, and (c) BW = 400 Hz; (d) mode number effects on the minimal detection value at BW = 1 Hz and BW = 100 Hz.

TABLE II. Comparison values of the first three resonance modes.

	Mode-1	Mode-2	Mode-3
f (Hz)	174 893.79	1 087 301.00	3 018 438.83
Q	14 696	11 409	8261
$f \cdot$ Q (Hz)	2.57×10^{9}	1.24×10^{10}	2.49×10^{10}
σ_{min}	5.078×10^{-8}	3.902×10^{-8}	1.192×10^{-8}
Δm (g)	6.6×10^{-19}	5.1×10^{-19}	1.5×10^{-19}

V. CONCLUSIONS

In summary, we demonstrated a higher-order mode actuated SCD resonator and analyzed the frequency stability by tracking the frequency fluctuation across the first three modes. The high-order mode resonances exhibited an exceptional performance in mass sensing, with the minimal detectable mass improving from 0.66 to 0.15 atto-gram (ag) utilizing the higher-order modes. These results highlight that sensing capability improves with increasing mode order. Operating the diamond sensor at higher order modes, with its superior frequency stability and enhanced minimal detection limits, offers a promising strategy for advanced sensing applications.

ACKNOWLEDGMENTS

This work was supported by JSPS KAKENHI (Grant Nos. 24KF0085, 24H00287, and 22K18957) and ARIM (Grant Nos. JPMXP1223NM5297), sponsored by the Ministry of Education, Culture, Sports, and Technology (MEXT) of Japan.

AUTHOR DECLARATIONS

Conflict of Interest

The authors have no conflicts to disclose.

Author Contributions

Wen Zhao: Conceptualization (equal); Data curation (lead); Formal analysis (equal); Investigation (lead); Methodology (equal); Resources (lead); Software (lead); Validation (equal); Visualization (equal); Writing – original draft (lead); Writing – review & editing (lead). **Guo Chen**: Investigation (supporting); Writing – original draft (supporting); Writing – review & editing (supporting). **Keyun Gu**: Investigation (supporting); Writing – original draft (supporting); Writing – review & editing (supporting). **Masaya Toda**: Investigation (supporting); Methodology (supporting); Writing – original draft (supporting); Writing – review & editing (supporting). **Yasuo Koide**: Writing – original draft (supporting); Writing – review & editing (supporting). **Meiyong Liao**: Conceptualization (lead); Data curation (equal); Formal analysis (equal); Funding acquisition (lead); Investigation (lead); Methodology (lead); Project administration (lead); Resources (lead); Software (lead); Supervision (lead); Validation (lead); Visualization (lead); Writing – original draft (lead); Writing – review & editing (lead).

DATA AVAILABILITY

The data that support the findings of this study are available from the corresponding author upon reasonable request.

REFERENCES

[1] N. V. Lavrik, M. J. Sepaniak, and P. G. Datskos, Rev. Sci. Instrum. **75**(7), 2229–2253 (2004).
[2] J. Fritz, M. K. Baller, H. P. Lang, H. Rothuizen, P. Vettiger, E. Meyer, H. -J Guntherodt, C. Gerber, and J. K. Gimzewski, Science **288**(5464), 316–318 (2000).
[3] D. Lange, C. Hagleitner, A. Hierlemann, O. Brand, and H. Baltes, Anal. Chem. **74**(13), 3084–3095 (2002).
[4] I. Voiculescu, M. E. Zaghloul, R. A. McGill, E. J. Houser, and G. K. Fedder, IEEE Sens. J. **5**(4), 641–647 (2005).
[5] C. Vančura, M. Rüegg, Y. Li, C. Hagleitner, and A. Hierlemann, Anal. Chem. **77**(9), 2690–2699 (2005).
[6] L. Wang, W. Zhao, and M. Younis, Sens. Actuators, A **379**, 115867 (2024).
[7] P. S. Waggoner and H. G. Craighead, Lab Chip **7**(10), 1238–1255 (2007).
[8] N. Hossain, M. Z. A. Mahmud, A. Hossain, M. K. Rahman, M. S. Islam, R. Tasnim, and M. H. Mobarak, Results Eng. **22**, 102115 (2024).
[9] Y. Yoon, I. Chae, T. Thundat, and J. Lee, Adv. Mater. Technol. **4**(3), 1800597 (2019).
[10] W. Zhao, N. Alcheikh, S. B. Mbarek, and M. I. Younis, J. Appl. Phys. **132**(14), 144502 (2022).
[11] W. Zhao, N. Alcheikh, F. Khan, U. Yaqoob, and M. I. Younis, Sens. Actuators, A **344**, 113688 (2022).
[12] W. Zhao, S. Ahmed, H. Fariborzi, and M. I. Younis, J. Micromech. Microeng. **31**(12), 125010 (2021).
[13] K. Park, N. Kim, D. T. Morisette, N. R. Aluru, and R. Bashir, J. Microelectromech. Syst. **21**(3), 702–711 (2012).
[14] S. K. Roy, V. T. K. Sauer, J. N. Westwood-Bachman, A. Venkatasubramanian, and W. K. Hiebert, Science **360**(6394), eaar5220 (2018).
[15] N. Hosseini, M. Neuenschwander, J. D. Adams, S. H. Andany, O. Peric, M. Winhold, M. C. Giordano, V. S. Bhat, M. Penedo, D. Grundler, and G. E. Fantner, Nat. Electron. **7**(7), 567–575 (2024).
[16] P. Sadeghi, A. Demir, L. G. Villanueva, H. Kähler, and S. Schmid, Phys. Rev. B **102**(21), 214106 (2020).
[17] S. A. Fedorov, N. J. Engelsen, A. H. Ghadimi, M. J. Bereyhi, R. Schilling, D. J. Wilson, and T. J. Kippenberg, Phys. Rev. B **99**(5), 054107 (2019).
[18] A. A. Basharin, V. Chuguevsky, N. Volsky, M. Kafesaki, and E. N. Economou, Phys. Rev. B **95**(3), 035104 (2017).
[19] L. Gu, W. Zhang, H. Lu, Y. Wu, and C. Fan, Microelectron. Eng. **271–272**, 111950 (2023).
[20] N. S. Gireesh, T. Sundararajan, and S. S. Gautam, Gyroscopy Navig. **11**(3), 206–213 (2020).
[21] D. D. Gerrard, C. H. Ahn, I. B. Flader, Y. Chen, E. J. Ng, Y. Yang, and T. W. Kenny, Presented at the 2016 IEEE 29th International Conference on Micro Electro Mechanical Systems (MEMS), 2016.
[22] K. Gu, Z. Zhang, G. Chen, J. Huang, Y. Koide, S. Koizumi, W. Zhao, and M. Liao, Carbon **225**, 119159 (2024).
[23] Z. Zhang, G. Chen, K. Gu, S. Koizumi, and M. Liao, Fun. Diam. **3**(1), 2221280 (2023).
[24] C. E. Nebel, Fun. Diam. **3**(1), 2201592 (2023).
[25] W. Zhao, S. Koizumi, and M. Liao, IEEE Electron Device Lett. **45**, 2268 (2024).
[26] L. Sang, H. Sun, X. Yang, T. Li, B. Shen, and M. Liao, Presented at the 2020 IEEE International Electron Devices Meeting (IEDM), 2020.
[27] M. Liao, Fun. Diam. **1**(1), 29–46 (2021).
[28] Z. Zhang, W. Zhao, G. Chen, M. Toda, S. Koizumi, Y. Koide, and M. Liao, Adv. Funct. Mater. **33**(27), 2300805 (2023).
[29] M. Liao, Y. Koide, and L. Sang, in *Novel Aspects of Diamond: From Growth to Applications*, edited by N. Yang (Springer International Publishing, Cham, 2019), pp. 91–121.
[30] M. Liao, M. Toda, L. Sang, T. Teraji, M. Imura, and Y. Koide, Jpn. J. Appl. Phys. **56**(2), 024101 (2017).
[31] H. Wu, L. Sang, Y. Li, T. Teraji, T. Li, M. Imura, J. You, Y. Koide, M. Toda, and M. Liao, Phys. Rev. Mater. **2**(9), 090601 (2018).
[32] W. Zhao, R. T. Rocha, N. Alcheikh, and M. I Younis, Mech. Syst. Signal Process. **196**, 110347 (2023).
[33] W. Zhao, F. Khan, N. Alcheikh, and M. I. Younis, IEEE Electron Device Lett. **43**(10), 1732–1735 (2022).
[34] D. Antonio, D. H. Zanette, and D. López, Nat. Commun. **3**(1), 806 (2012).
[35] M. Liao, M. Toda, L. Sang, S. Hishita, S. Tanaka, and Y. Koide, Appl. Phys. Lett. **105**(25), 251904 (2014).
[36] Y. Qiao, A. Elhady, M. Arabi, E. Abdel-Rahman, and W. Zhang, Microsyst. Nanoeng. **10**(1), 90 (2024).
[37] P. Neumann, I. Jakobi, F. Dolde, C. Burk, R. Reuter, G. Waldherr, J. Honert, T. Wolf, A. Brunner, J. H. Shim, D. Suter, H. Sumiya, J. Isoya, and J. Wrachtrup, Nano Lett. **13**(6), 2738–2742 (2013).
[38] T. A. Efimov, E. A. Rassolov, B. G. Andryukov, T. S. Zaporozhets, and R. V. Romashko, J. Phys.: Conf. Ser. **1439**(1), 012006 (2020).
[39] J. Verd, A. Uranga, G. Abadal, J. L. Teva, F. Torres, J. López, F. Pérez-Murano, J. Esteve, and N. Barniol, IEEE Electron Device Lett. **29**(2), 146–148 (2008).